A Planetary Wave Analysis Using the Acoustic and Conventional Arrays in the 1981 Ocean Tomography Experiment*

CHING-SANG CHIU

Woods Hole Oceanographic Institution, Woods Hole, MA 02543

YVES DESAUBIES

IFREMER, Centre de Brest, B.P. 337 Cedex, FRANCE

(Manuscript received 12 September 1986, in final form 2 March 1987)

ABSTRACT

Using the maximum likelihood estimation method, quasi-geostrophic wave solutions are fitted to the observations of the 1981 Ocean Acoustic Tomography Experiment. The experiment occupied a 300 km square area centered at 26°N, 70°W over a duration of approximately 80 days. The dataset consists of acoustic travel-time records, moored temperature records and CTD profiles. The acoustic data correspond to integral measurements of the temperature (or sound speed) field.

The optimal fit to the data corresponds to three waves in the first baroclinic mode, evolving under the presence of a westward mean flow with vertical shear. The mean flow is found to be weak (approximately 2 cm s^{-1}), but changes the wave periods significantly by producing large Doppler shifts. The waves are found to be dynamically stable to the mean flow, have weak nonlinear interactions with each other, and do not form a resonant triad; thus they constitute a fully linear solution.

Evidence for the existence of the waves is strongly supported by the high correlation (approximately 0.9) between the data and the fit, the large amount of signal energy resolved (approximately 80%), the excellent quality of the wave-parameter estimate (only about 10% in error), and the general agreement between the observations and quasi-geostrophic linear dynamics.

1. Introduction

Extensive studies of mesoscale motions in the last decade have shown that linear quasi-geostrophic dynamics are quite successful in the interpretation of a number of observations in the ocean. Under some general hypotheses pertaining to inviscid, incompressible, large-scale, low-frequency flows, the governing potential vorticity equation is obtained, which can be solved in terms of waves. Different wave classes are possible according to such factors as frequency, geometry or latitude. The various wave types are long gravity waves, Rossby (or planetary), Kelvin, topographic Rossby, equatorial, bottom trapped, etc. (LeBlond and Mysak, 1978; Pedlosky, 1979).

Although such waves are in theory plausible motions, they are difficult to observe in the ocean. This is in part because the long wavelengths and very low frequencies require large sensor arrays over long times and in part because if a superposition of waves is present in a broad spectrum, it becomes harder to identify the waves unambiguously. This latter difficulty is not specific to quasi-geostrophic flows, but also occurs in other random wave fields, such as surface gravity and internal waves. It becomes a subtle question to establish whether a random field is best described as a superposition of linear waves, weakly or strongly interacting nonlinear waves, or turbulence (Holloway, 1980).

If one assumes that the observed field is due to a superposition of randomly phased waves, characterized by a given spectrum, then a given wave type can be identified by its dispersion relation and by well-defined relationships between various components (such as temperature and velocity). Such relations have been called consistency relations (Muller and Siedler, 1976). The dispersion relation is a statement relating the spatial to the temporal behavior; thus the wave parameters, such as wave frequencies and wavenumbers, can be determined only by appropriate space–time observations.

A variety of observations of long waves has been reported in the literature; for example, baroclinic Rossby waves in the Pacific ocean from temperature surveys (Bernstein and White, 1974; Emery and Magaard, 1976; and White, 1977); topographic Rossby waves from mooring arrays (Thompson, 1971; Hogg, 1981); various types of equatorial trapped waves from mooring arrays (Eriksen, 1985; Weisberg et al., 1979); and island-trapped internal Kelvin waves from mooring arrays (Hogg, 1980).

* Woods Hole Oceanographic Institution Contribution Number 6254.

Although the existence of those waves has been convincingly demonstrated, direct observation in both space and time is much more difficult. A striking observation of a single barotropic wave was presented by Price and Rossby (1982). The analysis was done in terms of potential vorticity balance and the wave parameters were determined from the length and time scales of the correlation functions. The data were obtained from SOFAR floats drifting at 1300 m, a depth close to the null of the first baroclinic mode which thus could not be detected. The wave, found to have a Doppler-shifted period of 48 days, was observed during only the first 90 days of the experiment. McWilliams and Robinson (1974) analyzed data of the Soviet Polygon array in terms of a local, baroclinic, advective, topographic model of quasi-geostrophic waves in the presence of a mean current. Fits of one or two waves were made, but the results were not entirely convincing because the data used had already been strongly condensed by Koshlyakov and Grachev (1973). More complete and systematic fits of MODE-0 and MODE-1 array data were given by McWilliams and Flierl (1976). Here, the approach was more rigorous, since a least-squares estimate of the wave parameters was made, based on a large dataset covering space and time. Different combinations of baroclinic and barotropic waves were tried in an effort to expose the minimum of an error norm. In one case (MODE-0) two barotropic waves were found, and in the other (MODE-1) they found two barotropic and two baroclinic waves. However, the wave parameters they estimated may not be optimal in a statistical sense, since the weighting in the least-squares was not chosen according to the statistics of the errors in the data. Furthermore, they did not give any error maps on the estimated field.

An analysis similar to that of McWilliams and Flierl (1976) is presented here. The database comes from a combination of acoustic transmissions, CTD surveys and temperature moorings, covering a two and a half month period in a 300 km square at 26°N, 70°W, just south of the MODE region. The basic dataset was made available by the Ocean Tomography Group (1982) and has been presented by them as well as by Cornuelle (1983), Cornuelle et al. (1985) and Chiu (1985). In particular, Cornuelle et al. (1985) show that a cold eddy with temperature anomaly of −2°C was slowly moving to the west during the experiment.

However, the 1981 tomography experiment was mean essentially as a demonstration of a new acoustic technique, and accordingly the analysis of Cornuelle et al. (1985) chose purposefully to consider only the acoustic data, discarding other information available, such as dynamic considerations, other data, and time continuity. In contrast, we attempt here to see if the space–time behavior of the dataset can be interpreted in terms of a sum of baroclinic waves.

The assumption of waves automatically incorporates dynamical constraints on the fields and provides the required relationships between the various data subsets, as is outlined in section 2. A rigorous optimal estimation procedure of the wave parameters is outlined in section 3; it is equivalent to a weighted nonlinear least-squares procedure, leading to the minimization of an objective function.

Particular attention is paid to the estimation of the errors in the estimated wave parameters and on the reconstructed fields as well as on the figures of merit for the fits. The results of the estimation are discussed in section 4, where it is found that the least error is obtained by a model consisting of three baroclinic waves and a large-scale, weak, mean current. The waves are found to be stable and linear. Section 5 contains the conclusions and some final remarks. In particular, it will be seen that the wave assumption constitutes a convenient model for the analysis of such a diverse dataset. But a model can never be proven absolutely right: it can only be shown to perform better than many others, and its justification can only reside in its success to account for the data.

The analysis presented here gives strong evidence that baroclinic waves do exist and can be detected unambiguously; acoustic means are particularly well suited to the task because of the extensive space–time coverage they provide.

2. Observations and models

a. The experiment

The experiment was carried out in the spring of 1981 by the Ocean Tomography Group (1982). It occupied an area of 300 km by 300 km at 26°N, 70°W, a region on the Hatteras abyssal plain, southwest of Bermuda, and just south to where MODE was conducted. Figure 1 (from Cornuelle et al., 1985) shows the locations of

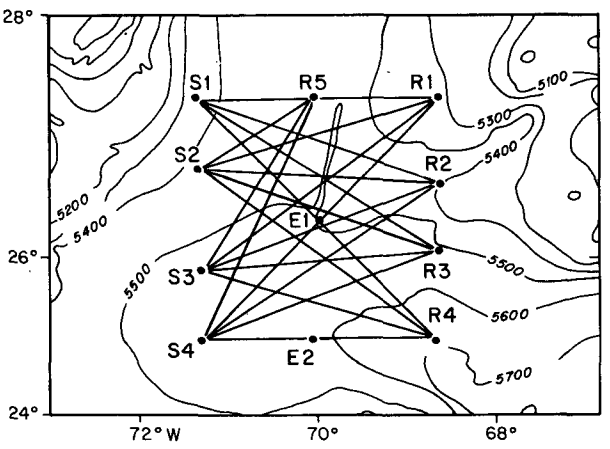

FIG. 1. The configuration of the 1981 Ocean Acoustic Tomography Experiment (from Cornuelle et al., 1985). The diagram shows the horizontal locations of the four source moorings (S1, . . . , S4), five receiver moorings (R1, . . . , R5), two environmental moorings (E1 and E2), and the bottom bathymetry.

the moorings, the horizontal paths of acoustic transmission and the bottom bathymetry. The monitored region has a nominal depth of 5400 m and very small depth variations.

The acoustic tomographic system consisted of a horizontal array of four sources (S1, . . . S4) and five receivers (R1, . . . R5) moored at a nominal depth of 2000 m surrounding the region under investigation (see Fig. 1). The average sound speed profile $\bar{c}(z)$ obtained from the CTD surveys in the experiment is shown in Fig. 2. As is typical of this part of the ocean, there is a deep sound channel allowing several eigenrays (multipaths) between a source and receiver (Fig. 3). Using a signal processing technique developed by Spindel (1979), a 224 Hz carrier modulated by a repetition of a maximal length, shift register sequence that lasted nearly three minutes was transmitted hourly on every third day between each of the source–receiver pairs. Through a form of matched filtering, the multipath travel times of acoustic pulses were estimated. The relation between travel time and sound speed changes, δt and δc, is approximately

$$\delta t = \int_x \frac{-\delta c}{\bar{c}^2} ds \tag{1}$$

where the integration is performed along the trajectory $\chi(s)$ of an eigenray, and s is the arc length along that ray. (The accuracy of this linear, approximate relation is discussed in appendix A.) Since a sound speed fluctuation δc is directly related to a temperature fluctuation δT by

$$\delta c = (4.6 - 0.11\bar{T} + 0.00087\bar{T}^2)\delta T \tag{2}$$

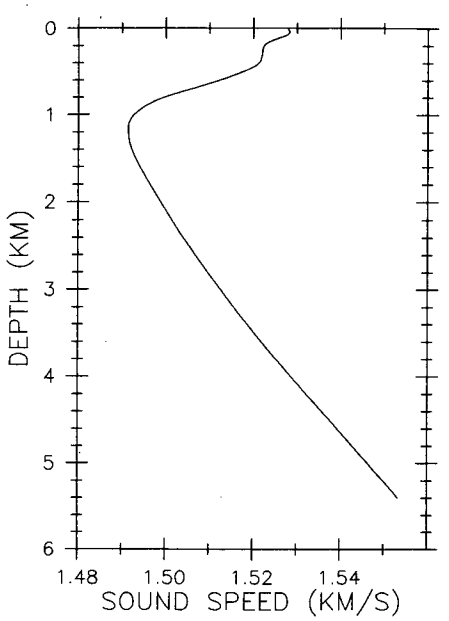

FIG. 2. The mean sound speed profile in the experimental region.

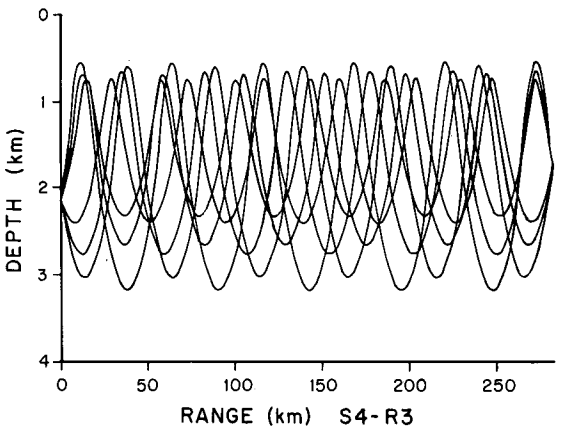

FIG. 3. The trajectories of six of the many eigen rays, connecting the source S4 to the receiver R3.

where $\bar{T}$ is the mean temperature, and where the units are m s^{-1} for sound speed and °C for temperature, these travel times correspond to spatially averaged measurements of the temperature perturbation field. [Note that (2) is obtained by differentiating the empirical formula of Medwin (1975) and neglecting the effects of salinity.]

Although the transmissions were intended to last for four months, more than half of the receivers had stopped recording data after 80 days into the experiment due to failure of the batteries. The motion of the acoustic moorings were tracked by bottom-mounted acoustic transponders. The tracking was needed to prevent the misinterpretation of the large changes in travel times due to mooring motion as changes due to oceanic perturbation.

In addition to the nine acoustic moorings, two environmental moorings, denoted by E1 and E2 in Fig. 1, were deployed. Current meters were mounted on the environmental moorings at two different depths but not on the acoustic moorings. A total of 32 temperature–pressure recorders and temperature sensors were distributed on all the moorings and mounted at different depths. Seven of them were placed in the energy-containing region of the baroclinic-mode waves, i.e. the main thermocline zone.

During the 80 day period in which the acoustic array was operational, two CTD surveys (in March and May) were conducted. Each CTD survey lasted two and a half weeks and had 65 casts distributed evenly over most of the experimental square, though slightly denser in the middle.

b. Data used

Because the barotropic mode produces little vertical displacement, waves in this mode are only observable through current measurements. The current data obtained in this experiment, however, are inadequate for

resolving the barotropic wave field because the current meters, located at two closely spaced spots, cannot provide sufficient spatial resolution. Our wave analysis is thus focused on the first baroclinic mode alone, which we have shown in a modal-decomposition analysis of the CTD data (presented in appendix B) to account for a major portion of the observed signal.

We take as our dataset seven moored sensor temperature time series, 58 travel-time records, and two CTD surveys. These measurements are most pertinent to the detection of planetary waves since they probe the energy-containing region of the waves, i.e. the main thermocline zone. Low-pass filtering is performed on the time records to eliminate tidal and internal-wave signals; furthermore, only data points on every third day in the moored temperature records and on every ninth day in the travel-time records are retained for the estimates. This reduction does not result in any loss of useful information, because the time scale of the midlatitude mesoscale motion is known to be of the order of 100 days (Richman et al., 1977). On the other hand, each CTD profile is compressed into a single datum a_j^0, where $a_j^0 \equiv d_{1j}$ is the amplitude of the first mode of sound speed perturbation in the jth profile as defined in appendix B. This compression of data corresponds to a filtering process in which the more oscillatory but less energetic higher modes are totally eliminated.

The dataset used in the parameter estimates is summarized in Table 1. For simplicity in the incorporation of different data types, we have chosen the sound speed perturbation, which is related to the temperature perturbation by (2), to be the unknown variable in the estimates. The seven moored sensor records of temperature, converted to sound perturbation time series via (2), were recorded only at three mooring sites, E1, E2 and S3, and are thus expected to contain mainly information on the time behavior of the perturbed field. In contrast, since the duration of each CTD survey is relatively short ($2\frac{1}{2}$ weeks) as compared to the wave period (of order 100 days), they should mainly contain spatial information. About three ray paths per source–receiver pair (which cycle through almost the entire depth of the main thermocline zone) were used. The corresponding time series records of travel time therefore contain information on both the time and space behavior of the perturbed field. Only the data obtained within the period between yeardays 61 and 139 were used since most of the acoustic instruments had failed after yearday 139 and the experiment started roughly on yearday 61. Thus the dataset contains information on the mesoscale perturbations that is densely sampled in both time and space in the 300 km square over a period of 80 days. We define the position 26°N, 70°W and the Julianday 66 in a Cartesian coordinate system as the point (150 km, 150 km, 0 s).

c. *Wave models*

Planetary wave motion can be affected by a number of factors, such as the presence or absence of a mean flow, a bottom slope, wave–wave interactions, etc. Depending on which of those effects are important, the corresponding perturbed field can display different space–time characteristics. Because there generally exists some degree of uncertainty as to which of those effects actually dominate in real situations, different but plausible dynamical models that place emphasis on different factors and are parameterized by different sets of wave parameters must be fitted to the data in a wave detection process. The actual dynamics can then be estimated by comparing the quality of the different model fits.

For the detection of baroclinic waves, we have estimated the wave and mean-flow induced sound speed perturbation $\delta c^m(\mathbf{x}, t; \mathbf{p})$ of three plausible wave propagation models, labeled 0, 1 and 2, using the dataset. The three models, their associated δc^ms as functions of position $\mathbf{x} = (x, y, z)$ and time t, where x, y and z are respectively the east, north and vertical coordinates, and the corresponding sets of wave parameters $\mathbf{p}$ are described next.

The geostrophic dynamic pressure, that is the mesoscale pressure deviation from the mean, can be cast into a sum of eigen modes:

$$p' = \sum_i \pi_i(x, y, t) f_i(z)$$

where f_i satisfies the vertical structure equation, rigid-lid boundary and orthonormal conditions [(B1)–(B3) in appendix B]. Flierl (1978) has shown that the evolution of the field is described by a set of coupled, nonlinear differential equations governing the amplitude functions of the modes. Neglecting surface forcing and

TABLE 1. Data used. In second column, j = index for position and k = index for time. Integer in parentheses in fifth column corresponds to the number of data in each time series.

Data type	Notation	Quantity	Duration (Julian days)	Number of data	Source
Modal amplitudes	a_j^0	65	66–83	65	1st CTD survey
Modal amplitudes	a_j^0	65	120–137	65	2nd CTD survey
δc time series	δc_{jk}^0	7	61–139	7 × (27)	Temperature sensors
δt time series	δt_{jk}^0	58	61–133	58 × (9)	Tomographic array

bottom topographic effects, and excluding modes higher than the first, these horizontal structure equations, which express potential vorticity conservation, are

$$L_0(\pi_0) = -C_0(\pi_1) - \frac{1}{\rho \bar{f}}[J(\pi_0, \nabla_h^2 \pi_0) + J(\pi_1, \nabla_h^2 \pi_1)]$$

$$L_1(\pi_1) = -C_1(\pi_0) - \frac{1}{\rho \bar{f}}\{\epsilon J(\pi_1, \nabla_h^2 \pi_1) + J(\pi_1, \nabla_h^2 \pi_0) + J[\pi_0, (\nabla_h^2 - \lambda_1)\pi_1]\} \quad (3)$$

where

$$L_0 = \frac{\partial}{\partial t}\nabla_h^2 + \beta\frac{\partial}{\partial x} + \left(u_0\frac{\partial}{\partial x} + v_0\frac{\partial}{\partial y}\right)\nabla_h^2$$

$$L_1 = \frac{\partial}{\partial t}(\nabla_h^2 - \lambda_1) + \beta\frac{\partial}{\partial x} + \left(u_0\frac{\partial}{\partial x} + v_0\frac{\partial}{\partial y}\right)(\nabla_h^2 - \lambda_1) + \epsilon\left(u_1\frac{\partial}{\partial x} + v_1\frac{\partial}{\partial y}\right)\nabla_h^2$$

$$C_i = \left(u_1\frac{\partial}{\partial x} + v_1\frac{\partial}{\partial y}\right)(\nabla_h^2 + \lambda_i) \quad i = 0, 1$$

are linear operators, ∇_h^2 denotes the horizontal Laplacian operator, J denotes the Jacobian nonlinear operator, ρ is a constant reference density (ρ = 1 g ml^{-1}), β is the latitudinal gradient of the Coriolis parameter, and

$$\epsilon = \frac{1}{D}\int_{-D}^{0} f_1(z)^3 dz. \quad (4)$$

A depth dependent mean current is represented in the horizontal structure equations by its amplitude components (u_0, v_0) in the barotropic mode and (u_1, v_1) in the first baroclinic mode. For this experiment, $\beta = 2.06 \times 10^{-8}$ km^{-1} s^{-1} and $\bar{f} = 6.38 \times 10^{-5}$ s^{-1}. By solving the eigenvalue problem (B1)–(B3), we get $\lambda_0 \approx 0$, $\lambda_1 = 5.15 \times 10^{-4}$ km^{-2}, and from (4), we obtain $\epsilon = 1.93$.

If we neglect the coupling and the nonlinear terms [rhs of (3)], the dispersion relation for the "primary" waves is

$$(k^2 + l^2 + \lambda_i)(\sigma + \delta\sigma) + k\beta = 0, \quad i = 0, 1 \quad (5)$$

where

$$\delta\sigma = -(u_0 k + v_0 l), \quad \lambda_0 \approx 0$$

for the barotropic mode (i = 0), and

$$\delta\sigma = -\left[k\left(u_0 + \epsilon\frac{k^2 + l^2}{k^2 + l^2 + \lambda_1}u_1\right) + l\left(v_0 + \epsilon\frac{k^2 + l^2}{k^2 + l^2 + \lambda_1}v_1\right)\right] \quad (6)$$

for the first baroclinic mode (i = 1), and where (k, l) is the wavenumber vector, σ the wave frequency, and $-\delta\sigma$ the Doppler shift.

One might expect a priori that the coupling terms $C_i(\pi_i)$ should be of the same order as the linear terms $L_i(\pi_i)$; it will be shown a posteriori in section 4 that they are negligible. Therefore, it is justified to use the simplified dispersion relation (5). On the other hand, the nonlinear terms give rise to wave–wave interaction, which can lead to the generation of "secondary" waves (Longuet-Higgins et al., 1967). At resonance, when the wavenumber vector and frequency of the secondary wave also satisfies (5), its amplitude can grow (or decay) in time. This possibility is allowed for in one of our models. Three models are considered.

Model 0

This model consists of freely propagating first baroclinic-mode Rossby waves in the absence of a mean flow. The isopycnal surfaces are displaced by the baroclinic waves so that the corresponding local sound speed perturbations are given by

$$\delta c^m(\mathbf{x}, t; \mathbf{p} = \mathbf{p}^w) = \delta c^w(\mathbf{x}, t; \mathbf{p}^w)$$

with

$$\delta c^w = g_1(z)\sum_{i=1}^{W} A_i \cos(k_i + l_i - \sigma_i t + \gamma_i) \quad (7)$$

where W is the number of first baroclinic-mode waves, and $g_1(z)$ is the corresponding vertical mode, which is displayed in Fig. 4 together with the second and third modes. The amplitude A_i, the wavenumber vector (k_i, l_i), the frequency σ_i and the phase constant γ_i of the ith wave are wave parameters. In this model $\delta\sigma$ = 0,

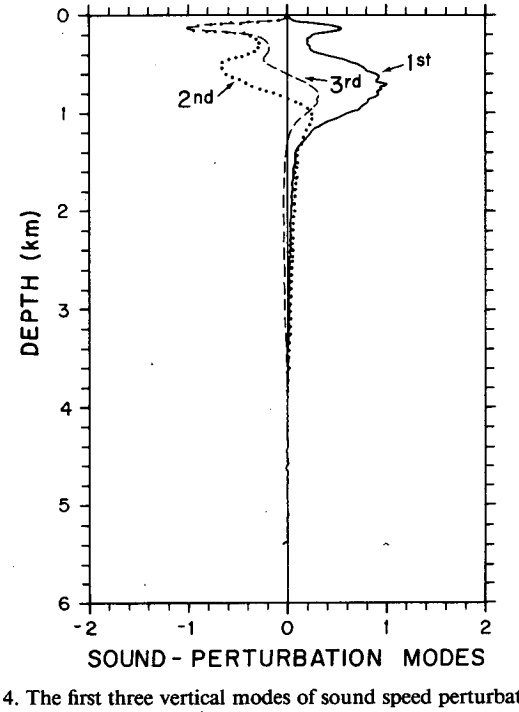

FIG. 4. The first three vertical modes of sound speed perturbation.

and σ_i, being constrained by (k_i, l_i) according to (5), is not a free parameter; thus δc^w is completely determined by

$$\mathbf{p}^w = (A_1, k_1, l_1, \gamma_1, \cdots, A_W, k_W, l_W, \gamma_W).$$

Model 1

The possibility of a mean flow is now added. The structure of the mean current is assumed to consist of the barotropic and the first baroclinic modes only. This assumption is probably a good one because the two modes are known to contain the greatest fraction of the kinetic energy in this general area (McWilliams and Flierl, 1975, and Sanford, 1975). In this model the isopycnal surfaces are further tilted by the baroclinic mean current according to the thermal wind relation. Therefore, the corresponding sound speed perturbations are now given by

$$\delta c^m = \delta c^w(\mathbf{x}, t; \mathbf{p}^w, u_0, v_0, u_1, v_1) + \delta c^c(\mathbf{x}; u_1, v_1, b_0)$$

with an additional time-independent mean variation

$$\delta c^c = g_1(z)\left(b_0 - \frac{u_1}{F}\cdot\frac{y}{D} + \frac{v_1}{F}\cdot\frac{x}{D}\right)$$

where F is a known constant determined by the thermal-wind relation and the normalization used on the vertical modes ($F = 0.157$), and b_0 is a constant arising from integrating the derivative relation between the mean flow and the stream function δc^c; this constant shifts the null of δc^c to the correct position. The frequency shift $\delta\sigma$ in (6) now exists and is constrained by (k, l), (u_0, v_0) and (u_1, v_1). Thus, δc^m is now parameterized by

$$\mathbf{p} = (\mathbf{p}^w, u_0, v_0, u_1, v_1, b_0).$$

Of course, the perturbations and effects caused by the mean flow and waves of much larger scales and lower frequencies are locally indistinguishable. It is therefore more accurate to refer to δc^c as a local mean, that is, the sum of the perturbations induced by the mean flow and much longer waves.

Model 2

The possibility of resonant wave–wave interaction is now included. The modeling requires the replacement of A_i by $A_i + G_i t$ in (7) where G_i represents the growth rate. In general, the growth rates are constrained by the wavenumbers and wave amplitudes of the interacting primary waves (Longuet-Higgins et al., 1967). However, since the barotropic mode is not observable in our dataset while resonant waves can be generated by intermodal wave–wave interactions (Chiu, 1985), G_i can only be left as a free parameter in the model. The set of parameters are now given by

$$\mathbf{p} = (\mathbf{p}^w, G_1, \cdots, G_W, u_0, v_0, u_1, v_1, b_0).$$

3. Estimator

Maximum likelihood is a widely used method for estimation, because it is simple to apply and the estimates are generally easy to compute. Also, the maximum likelihood estimate, in a sense, is robust, since many other common estimators give the same estimate when all the random variables under consideration are assumed to have normal statistics (Tarantola and Valette, 1982; Cornuelle, 1983; and Chiu, 1985).

The maximum likelihood estimator can be formulated as the minimization of an objective function, the likelihood function (Bard, 1974). Grouping the 130 modal-amplitude data

$$(a_j^0; j = 1, \cdots, 130),$$

the seven observed time series of sound speed perturbations

$$[\delta c_{jk}^0 = \delta c_j^0(t = 3k\,\text{days}); k = 0, \cdots, 26; j = 1, \cdots, 7]$$

and the 58 observed time records of travel-time perturbations

$$[\delta t_{jk}^0 = \delta t_j^0(t = 9k\,\text{days}); k = 0, \cdots, 8; j = 1, \cdots, 58]$$

as three subsets of data (refer to Table 1 for the sources of data and notation), and further treating the uncertainty in the nominal horizontal positions, $\Delta\mathbf{x}$, and the unknown horizontal displacements

$$[\delta\mathbf{x}_k = \delta\mathbf{x}(t = 9k\,\text{days}); k = 0, \cdots, 8]$$

of the acoustic moorings as random parameters, the objective function can be cast as a sum of five constraining functions of similar forms of weighted sums of squares of residuals. Because there were nine acoustic moorings, $\Delta\mathbf{x}$ and $\delta\mathbf{x}_k$ are 18-dimensional vectors, and we denote their jth components by Δx_j and δx_{jk}, respectively. The objective function can thus be expressed as

$$\begin{aligned} s(\mathbf{p}, \Delta\mathbf{x}, \delta\mathbf{x}_0, \cdots, \delta\mathbf{x}_8) &= s_a(\mathbf{p}) + s_{\delta c}(\mathbf{p}) + s_{\delta t}(\mathbf{p}, \Delta\mathbf{x}, \delta\mathbf{x}_0, \cdots, \delta\mathbf{x}_8) \\ &\quad + s_{\Delta x}(\Delta\mathbf{x}) + s_{\delta x}(\delta\mathbf{x}_0, \cdots, \delta\mathbf{x}_8) \end{aligned} \quad (8)$$

with

$$s_a = \frac{1}{2}\sum_{j=1}^{130} \sigma_{a_j}^{-2}[a_j^0 - a_j^m(\mathbf{p})]^2 \quad (9)$$

$$s_{\delta c} = \frac{1}{2}\sum_{j=1}^{7}\sum_{k=0}^{26} \sigma_{\delta c_{jk}}^{-2}[\delta c_{jk}^0 - \delta c_{jk}^m(\mathbf{p})]^2 \quad (10)$$

$$s_{\delta t} = \frac{1}{2}\sum_{j=1}^{58}\sum_{k=0}^{8} \sigma_{\delta t_{jk}}^{-2}[\delta t_{jk}^0 - \delta t_{jk}^m(\mathbf{p}, \Delta\mathbf{x}, \delta\mathbf{x}_k)]^2 \quad (11)$$

representing the constraints imposed by each of the data subsets on a wave propagation model (Model 0, 1 or 2), where a_j^m, δc_{jk}^m and part of δt_{jk}^m are the signals produced by the waves and mean flow. Note that the other part of δt_{jk}^m is the perturbation related to the un-

certainties in the mooring positions; the mathematical models for all these signals and the parameterization of the mooring position errors in the model of travel-time signal are presented in appendix C. Furthermore,

$$s_{\Delta x}=\frac{1}{2}\sum_{j=1}^{18}\sigma_{\Delta x_j}^{-2}\Delta x_j^2 \tag{12}$$

$$s_{\delta x}=\frac{1}{2}\sum_{j=1}^{18}\sum_{k=0}^{8}\sigma_{\delta x_{jk}}^{-2}\delta x_{jk}^2 \tag{13}$$

represent the constraints on the incorrect horizontal mooring positions. We have assumed uncorrelated and normally distributed experimental noise and mooring-position errors with known variances; the variances of a_j^0, δc_{jk}^0, δt_{jk}^0, Δx_j and δx_{jk} are denoted by $\sigma_{a_j}^2$, $\sigma_{\delta c_{jk}}^2$, $\sigma_{\delta t_{jk}}^2$, $\sigma_{\Delta x_j}^2$ and $\sigma_{\delta x_j}^2$, respectively. The assignment of these noise variances is described below.

By analyzing numerous sound speed profiles acquired by Piips (1967) between Bermuda and Eleuthera, Mooers (1975) found strong evidence for the existence of a first baroclinic semidiurnal tide with an amplitude of 0.7 m s^{-1} in δc at 550 m depth. Higher-mode perturbations of approximately the same order, as estimated from decomposing the CTD profiles, are neglected in all three wave propagation models. These neglected higher-mode perturbations, combined with the internal tide, are the major contributors to model error. Another significant contributor to error is the random field of internal waves. While the errors in the modal-amplitude data are most sensitive to the internal tide and waves due to the lack of temporal filtering, the errors in the filtered δc time records are most sensitive to higher-mode fluctuations. In addition, the δc time records are also subject to errors caused by vertical mooring motion. We estimate both the $\sigma_{\delta c_{jk}}$ and σ_{a_j} to be approximately 1 m s^{-1}.

Considering only measurement noise, internal waves, and tides, Cornuelle et al. (1985) have estimated the daily mean variance of travel-time noise to be 3.6 $(\text{ms})^2$. Through computer simulations, we have estimated the error introduced by the neglected higher-mode perturbations and current effects, and the assumption of travel-time linearity (1) in our models, to be 5 ms (rms). Therefore, the total travel-time variance is $\sigma_{\delta t_{jk}}^2 = 3.6 + 25\ (\text{ms})^2$.

The tracking data provided by the acoustic bottom transponders indicate that the horizontal mooring displacements were of order 200 m rms. These tracking records had already been applied to eliminate the signal produced by some of the mooring motions in the travel-time data. However, these records contain large gaps resulting from occasional malfunction of the instruments. Therefore, we have set $\sigma_{\delta x_{jk}} = 200$ m and 20 m for the untracked and tracked displacements, respectively. The 20 m standard deviation represents the measurement error expected from the tracking system. We have further set $\sigma_{\Delta x_j} = 500$ m for all j, which is estimated from the differences between the observed travel times and the raytrace travel times calculated using the uncorrected mooring positions.

Due to the highly nonlinear nature of the objective function (8), a stable, iterative descent method developed by Fletcher and Powell (1963) was chosen for the optimization. An advantage of this method is that it also computes an estimate of the matrix of second derivatives (known as the Hessian $\mathbf{H}$) at the minimum, which is related to the local curvature. Bard (1974) has shown that by approximating the posterior distribution of the parameters with a normal distribution, the covariance matrix of the error $\mathbf{e}$ of the estimate $\hat{\mathbf{u}} \equiv (\hat{\mathbf{p}}, \widehat{\Delta \mathbf{x}}, \widehat{\delta \mathbf{x}_0}, \ldots)$ of $(\mathbf{p}, \Delta \mathbf{x}, \delta \mathbf{x}_0, \ldots)$ becomes

$$C_{\mathbf{e}} = \mathbf{H}^{-1}. \tag{14}$$

Thus, the diagonal elements in the inverse Hessian $\mathbf{H}^{-1}$ at the minimum are approximately the mean square errors of the estimates of the parameters.

If a model is accurate and parameters are well determined, the residuals will reflect the experimental random noise and have approximately the same statistics. Therefore, the reliability of a model can be assessed by analyzing the final residuals. To compare the goodness of the different wave models, we use a simple yet very useful measure, which is a weighted sum of the final residuals, defined as

$$R=\frac{m+r}{m-n}[s_a(\hat{\mathbf{p}})+s_{\delta c}(\hat{\mathbf{p}})+s_{\delta t}(\hat{\mathbf{u}})] \tag{15}$$

where R is approximately a chi-square distributed random variable with m degrees of freedom, r is the number of mooring-position parameters, n is the number of wave parameters, and m is the number of data. The factor $(m + r)/(m - n)$ is needed to adjust the inverse covariance matrix of noise to equal that of the final residuals (Bard, 1974). A significance level can be selected for rejecting models on the higher edge of the distribution.

Two other measures are used here to judge the success of a model in predicting (interpolating) the data. They are the correlation coefficient C between observed and predicted signal and the amount of signal energy E (in percentage) resolved by the prediction. The larger C and E are, the better the model fits the data. The similarities in shape and amplitude between the observed signal and the model prediction are measured by C and E, respectively. In general, C and E are independent, but for a least-squares minimization, $100C = E^{1/2}$ for the total set of data points. However, for individual subsets of data, C and E remain useful separate pieces of information.

4. Results and discussion

For each of the three models, one to five waves were fitted to the data. At least four different initial guesses

of **p** for a given model (Model 0, 1 or 2) and a given number of waves (W = 1, 2, 3, 4, or 5) were used in the optimizations to explore the least minimum (i.e. the solution) and to investigate uniqueness. This is needed because the objective function (8) is nonquadratic and thus more than one minimum could exist in the acceptable region in the solution space. While the wave fits with $W \leq 3$ are unique, those with $W > 3$ are not. In each fit with $W \leq 3$, most of the initial guesses converged to the same stationary point where the least minimum occurs, and although a few initial guesses converged to different stationary points, the corresponding minima are considerably larger. For each of the wave fits with $W > 3$, different initial guesses resulted in different minima of approximately the same size; hence a unique least minimum could not be identified. However, this has no effect on our investigation, because the optimal fit corresponding to $W = 3$ was unique and well-determined.

The change from uniqueness to nonuniqueness as W increases is a demonstration of the trade-off between resolution and stability (Backus and Gilbert, 1970). As W increases, so do the magnitudes of the wavenumber estimates. Thus, finer-scale structures of the perturbations are intended to be resolved with a larger W, but because of the inadequacy of the data in resolving them, the observing system is rendered underdetermined.

In order to assess and compare the different wave fits so that the optimal model and W may be identified, the weighted sum of the squares of final residuals R, defined in (15), was computed for each of the wave fits. The 0.01 significance level is at $R \approx 940$. In Fig. 5, we plot R versus W for each model. It is seen that the performance of Models 1 and 2 is much better than that of Model 0. While none of the wave fits of Model 0 pass the 0.01 significance test, the fits with W = 3, 4 and 5 of Model 1 and 2 are at and beyond the 0.01 significance level. Although Model 1 and 2 perform equally well, the estimated growth rates of the wave amplitudes in Model 2 do not differ significantly from zero and, in fact, their signs are ambiguous because their rms errors are larger than the estimated growth rates themselves. The lack of ability to determine the growth rates is not surprising, however, because (i) resonant interactions should be rare occurrences since the forced waves can grow if and only if they satisfy the dispersion relationship (5), and (ii) even if resonance actually occurs, the time scale of the growth, in weak-interaction theory, is much longer than a wave period; hence, data measured within a wave period cannot be adequate for observing such phenomena. The reason for fitting Model 2 to the data is to see if there are any surprises that are inconsistent with the theory. The data variance resolved by Model 1 increases by 20% as W changes from 2 to 3 and increases by as little as 5% as W further changes from 3 to 4 or 5. Also, we must keep in mind that W = 4 and 5 correspond to unstable

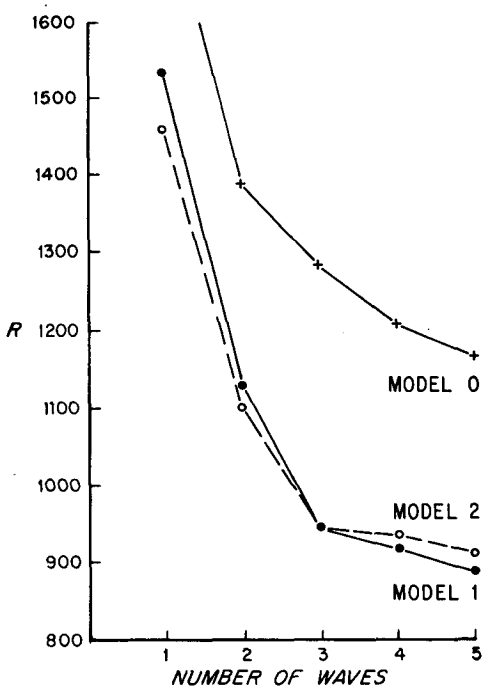

FIG. 5. Misfits of the three wave models on the data as functions of the number of wave(s) fitted. The measure of misfit is R, a weighted sum of the squares of final residuals.

wave fits. Thus, an overall judgment clearly favors Model 1 to be the optimal wave propagation model in which a mean flow is present and W = 3 to be the optimal number of propagating first baroclinic-mode waves.

To make further assessments, we computed for each wave fit the correlation coefficient C_i between each subset of data and the fit, and the amount of variance in each data subset resolved by the fit, E_i, where the index i takes on the integer values 1, 2 and 3 to denote the data subsets of modal amplitudes, δc time records and δt time records, respectively. For Model 1, that is the optimal model, C_i and E_i versus W are plotted in Figs. 6 and 7, respectively. At W = 3, i.e. the optimum, we obtain C_i of 0.8, 0.9 and 0.98 and E_i of 78, 82 and 96% for i = 1, 2 and 3, respectively. Although C_3 and E_3 are considerably larger, there is no inconsistency because a large portion of the variance in the δt time records is resolved by the determination of the mooring-position errors alone. The consistently high correlations and percentage of the signal resolved are a strong evidence of the existence of three first baroclinic-mode planetary waves in the region during the experimental period. The optimal values of the parameters for the waves and mean flow, and their rms errors (square roots of the diagonal elements of $\mathbf{H}^{-1}$) are shown in Table 2; the phase and group velocities, the Doppler shifts, and the wave periods themselves, as well as the directions and lengths of the waves are presented. Although the mean flow is very weak, it must be taken

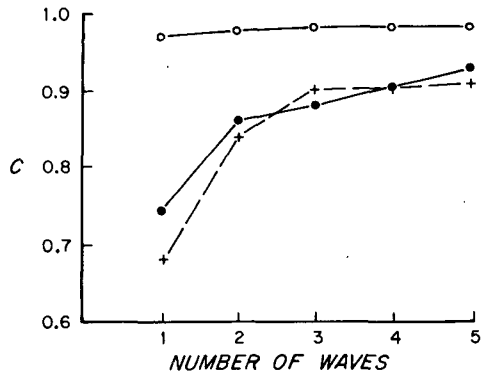

FIG. 6. Correlations of the travel-time perturbation records (O), the moored temperature-perturbation records (+) and the observed modal-amplitudes from CTD surveys (●) with the Model 1 fit for a given number of wave(s).

into consideration, since it accelerates the phase propagation considerably by generating Doppler effects; it is thus vital to the success of the wave fit.

The seven time records of δc observed from the moored temperature sensors are plotted in Fig. 8 together with the optimal fit. It is seen that the observations and the optimal interpolations compare favorably. Furthermore, some secondary perturbations with a period of about 20 days superimposed on the primary wave perturbations are found consistently in all the time records. The secondary oscillations were most profound at the mooring site E2, i.e. at $(x, y) = (150.7, 13.6)$ km. Because the frequency is below the inertial frequency, this oscillation cannot be due to internal waves; we speculate that the secondary perturbations were caused by the forced waves that oscillate at frequencies equal to the sum of the frequencies of the interacting barotropic and/or baroclinic waves. As observed in Fig. 8, the model errors are not exactly independent at every time point. Thus, the wave fit probably slightly overestimates its own accuracy due to the assumption of uncorrelated experimental noise.

To demonstrate that the observed pattern of the fairly complicated system can indeed be reconstructed accurately by the gradual evolution of three waves, we show a time sequence of contour maps of the estimated sound speed perturbation at a depth of 700 m in Fig. 9. The observed sound speed from the first and second CTD surveys at the same depth are contoured in Fig. 10 for comparison. It is seen that the waves generated a trough that was moving slowly to the west and then produced a front that was advancing from the northeast during the later period.

The covariance matrix $\mathbf{H_p}^{-1}$ of the wave-parameter estimate $\hat{\mathbf{p}}$ (i.e. the corresponding block in the inverse Hessian matrix of the objective function evaluated at the minimum point) gives indications of which wave parameters, or linear combinations of wave parameters, are well-determined, and which are poorly determined. A simple measure of the quality of the estimate is given by the diagonal elements of $\mathbf{H_p}^{-1}$, which are the mean square errors of the estimate; the rms errors are listed in Table 2. Using $\mathbf{H_p}^{-1}$, we can also obtain an error estimate of the estimated sound speed perturbation $\widehat{\delta c} = \delta c^m(\hat{\mathbf{p}})$ due to the error $\mathbf{e}$ of the estimated wave parameters $\hat{\mathbf{p}}$. Through a linearization of the wave and mean-flow induced sound speed perturbation $\delta c^m(\mathbf{p})$ about $\hat{\mathbf{p}}$, the error of $\widehat{\delta c}$ can be approximated by

$$\Delta\widehat{\delta c} \approx \left[\frac{\partial}{\partial \mathbf{p}} \delta c^m(\hat{\mathbf{p}})\right]^T \mathbf{e}.$$

It then follows that the mean square error of $\widehat{\delta c}$ can be expressed as

$$\langle \Delta\widehat{\delta c}^2 \rangle \approx \left[\frac{\partial}{\partial \mathbf{p}} \delta c^m(\hat{\mathbf{p}})\right]^T \mathbf{H_p}^{-1} \left[\frac{\partial}{\partial \mathbf{p}} \delta c^m(\hat{\mathbf{p}})\right]. \quad (16)$$

In Fig. 11, we show the contour plots of the rms error [i.e., the square root of the variance (16)] of the sound speed perturbation estimate as displayed in Fig. 9. Because the densities of the ray paths and the CTD stations were much higher in the middle of the area, the errors are smaller there. Furthermore, since there was an environmental mooring E2 on the southern boundary, the errors near this boundary are smaller than those near the northern boundary where no environmental mooring was deployed (see Fig. 1). The constraint imposed by the wave dynamics introduces a high correlation between the sound speed perturbations at different locations and times; thus the errors in all the maps stay within a narrow range.

Westward phase propagation is known to be typical of mesoscale perturbations at midlatitudes. Consistently, as indicated in Table 2, the phases of the observed waves were all propagating westward. The corresponding group-velocity vectors also have westward

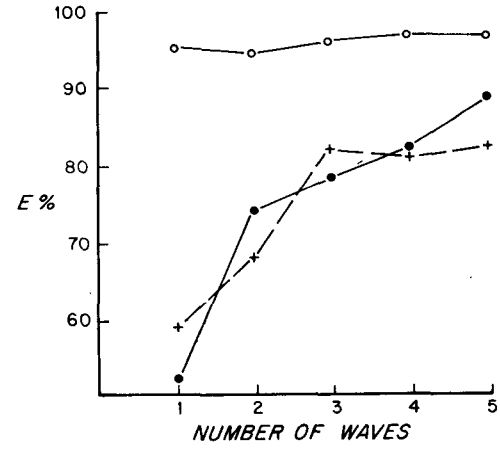

FIG. 7. Amounts of variance accounted for in the travel-time perturbation records (O), moored temperature-perturbation records (+) and the observed modal-amplitudes from CTD surveys (●) by the Model-1 fit for a given number of wave(s).

TABLE 2. Optimally estimated wave parameters. The numbers after the ± signs are rms errors.

a. Independent wave parameters

Wave (i)	δc amplitude A_i (m s^{-1})	Wavenumber vector k_i (km^{-1})	Wavenumber vector l_i (km^{-1})	Phase constant γ_i (rad.)	Mode (m)	Mean-current modal-amplitude vector u_m (cm s^{-1})	Mean-current modal-amplitude vector v_m (cm s^{-1})	Reference δc b_0 (m s^{-1})
1	1.10 ± 0.13	−0.0118 ± 0.0011	0.0203 ± 0.0010	2.13 ± 0.19	0	−1.70 ± 0.24	0.11 ± 0.08	
2	2.28 ± 0.12	−0.0066 ± 0.0005	−0.0198 ± 0.0007	1.51 ± 0.12	1	−0.76 ± 0.13	0.39 ± 0.09	−1.46 ± 0.21
3	1.73 ± 0.09	−0.0119 ± 0.0005	−0.0034 ± 0.0008	−0.06 ± 0.11				

b. Dependent wave parameters

Wave (i)	Wave length (km)	Direction of phase (deg)	Wave period (days)	Doppler-shifted period (days)	Phase velocities (cm s^{-1}) Eastward	Phase velocities (cm s^{-1}) Northward	Group velocities (cm s^{-1}) Eastward	Group velocities (cm s^{-1}) Northward
1	268	120	117	−202	−5.25	3.06	−4.24	0.23
2	300	−108	344	−164	−3.19	−1.06	−4.30	1.16
3	509	−164	121	−77	−5.04	−17.69	−4.23	0.53

directions, implying that the waves were generated somewhere to the east of the experimental region; therefore, the possibility that they were radiated by the intense Gulf Stream can be ruled out. The three baroclinic waves do not form a resonant triad since the sum or difference of the phases of two of the waves does not equal the phase of the other wave. However, the propagation of resonant baroclinic waves is still possible because they could be generated by interacting barotropic waves. The fastest oscillation that could be forced by the observed baroclinic waves would result from the interaction between the first and the third waves and would have a period of $(1/117 + 1/121)^{-1} \approx 60$ days. But, since the secondary perturbation which we have observed from the moored time records of temperature has a period of 20 days (see Fig. 8), it must be due to the interaction of barotropic waves that have much higher frequency cutoffs.

In the absence of a mean flow, the short-period cutoff of the first baroclinic-mode waves is approximately 160 days, and thus cannot account for the faster oscillations of period 120 days in the data. This is well demonstrated by the poor fits of Model 0. Although the mean current, as estimated, is very weak (approximately 2 cm s^{-1}), it strongly alters the space and time behavior of the wave-induced perturbations by producing large changes in the wave periods or frequencies (the Doppler effects have reduced the wave periods of the three waves by 202, 164 and 77 days, respectively). Thus, the weak mean current has played an important role in the wave propagation in the region.

The approximate solution for linear dispersive planetary waves is obtained by neglecting the nonlinear and linear-coupling terms in the horizontal-structure equations (3) for mesoscale motions. Let us first comment on the linearization and then discuss the linear coupling in the context of stability theory. Qualitatively, the linearization is valid when the ratio of the particle to phase speed of the waves is small when compared to unity. As the ratio decreases, so do the nonlinear effects. Therefore, by shortening the wave periods and hence increasing the phase velocities, a westward mean current can weaken the nonlinear interactions between the dispersive waves, thus making the linear approximation better. The magnitudes of the phase and particle velocities of the observed dispersive primary waves were computed and the results are presented in Table 3. Furthermore, the magnitudes of the phase velocities of the waves, computed as if the mean current were absent, are also presented in the same table. It is seen that if the weak mean current were absent, the validity of the linearization for the wave motions would be harder to justify. The pressure amplitudes of the secondary waves forced by the observed primary waves and the pressure amplitudes of the primary waves themselves are given in Table 4. The ratios of the rms pressure amplitudes of the secondary to the primary waves are approximately 1/4. Thus, there could be up to a 25% error in the linear model.

Since we have observed a horizontally stratified flow with vertical shear, we shall investigate the stability of the flow in the presence of wave disturbances. The corresponding instability phenomenon is baroclinic. When it occurs, the available potential energy of the sloping-isopycnal mean state is converted to the potential and kinetic energy of the perturbations. A consequence of baroclinic instability is that the wave disturbances will grow and the tilted mean-state isopycnal surfaces will become more horizontal, that is, warm fluid will rise and cold fluid will sink.

Mathematically, the linear couplings in (3) give rise to baroclinic instability. After dropping the nonlinear

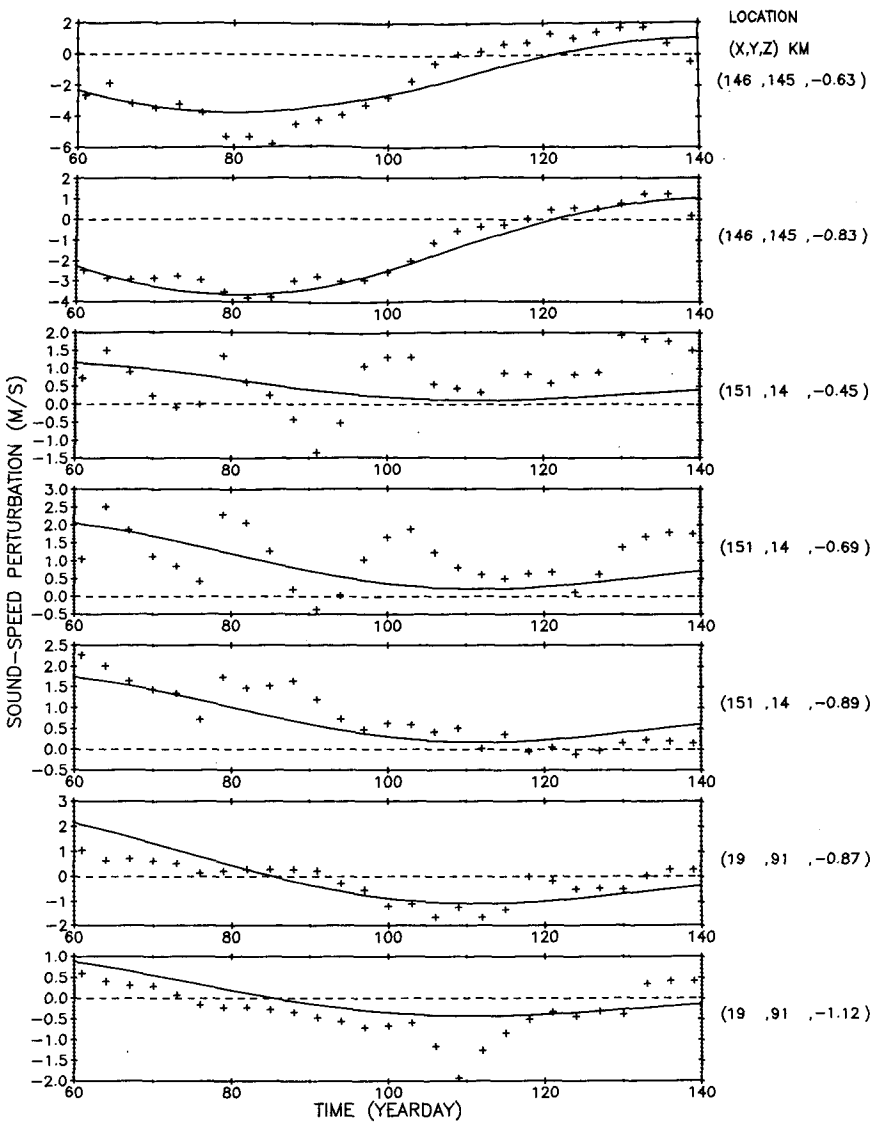

FIG. 8. Comparison of the optimal wave fit (solid lines) with the sound speed perturbation time series (+++) observed from the temperature sensors moored at seven different locations.

terms and performing a triple Fourier transformation, (3) can be cast as an eigenvalue problem in matrix algebra:

$$\begin{pmatrix} a_{11} & a_{12} \\ a_{21} & a_{22} \end{pmatrix} \begin{pmatrix} \Pi_0 \\ \Pi_1 \end{pmatrix} = \sigma \begin{pmatrix} \Pi_0 \\ \Pi_1 \end{pmatrix}$$

with

$$a_{11} = \frac{-\beta k}{k^2+l^2} + (u_0 k + v_0 l)$$

$$a_{22} = \frac{-\beta k}{k^2+l^2+\lambda_1} + (u_0 k + v_0 l) + \epsilon(u_1 k + v_1 l)\frac{k^2+l^2}{k^2+l^2+\lambda_1}$$

$$a_{12} = u_1 k + v_1 l$$

$$a_{21} = (u_1 k + v_1 l)\frac{k^2+l^2-\lambda_1}{k^2+l^2+\lambda_1}$$

where $\Pi_0(k, l, \sigma)$ and $\Pi_1(k, l, \sigma)$ are the spectra of the modal-amplitude functions of the zero and first mode perturbation pressures, respectively. For a given wavenumber vector (k, l), the wavefrequencies σ, i.e., the eigenvalues, are given by

$$\sigma_{\pm}(k,l) = \frac{a_{11}+a_{22} \pm [(a_{11}-a_{22})^2 + 4a_{21}a_{12}]^{1/2}}{2}.$$

Note that the coupling is caused by the baroclinic mean current only, and when coupling is neglected σ_- and

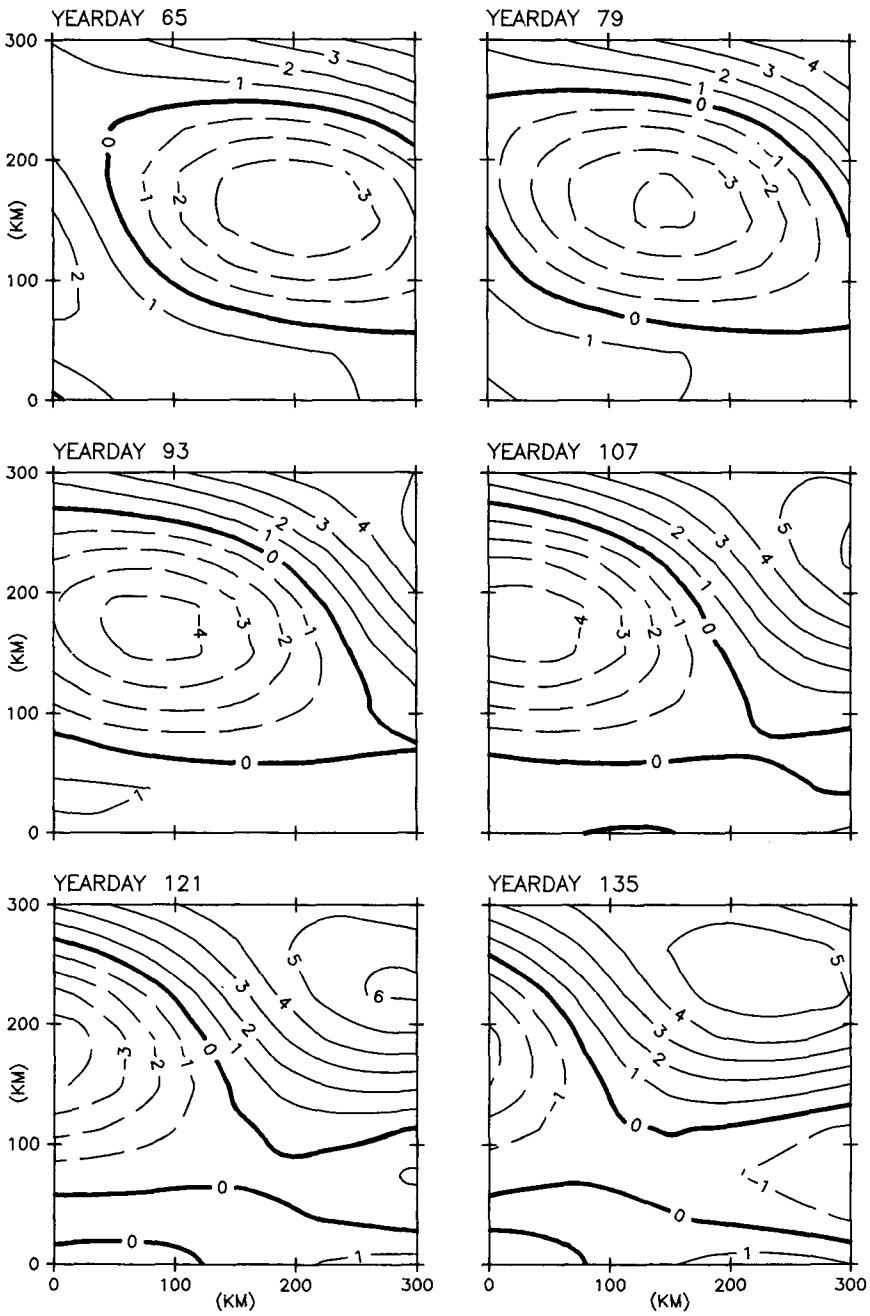

FIG. 9. A time sequence of maps of sound speed perturbation (in m s^{-1}) at a depth of 700 m of the optimally estimated wave field.

σ_+ are the same as the frequencies of the dispersive barotropic and baroclinic waves, respectively. It can be checked that with the values given in Table 2, $\sigma_- \approx a_{22}$, thus justifying (5).

For disturbances with (k, l) satisfying

$$(a_{11} - a_{22})^2 < -4a_{12}a_{21},$$

the wavefrequencies are complex. Under this condition, since σ_+ and σ_- are complex conjugates, one of them must have a positive imaginary part that corresponds to instability.

The shaded area on the k–l plane displayed in Fig. 12 is the region of instability. In the figure, we also plot the locations of the observed wave disturbances, which are seen to be stable. However, we must warn that, as the waves approach the western boundary, they may

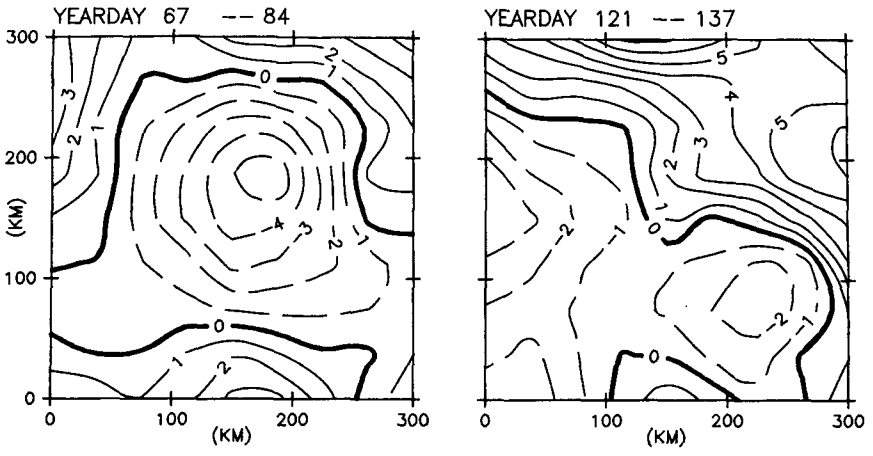

FIG. 10. Sound speed perturbations (in m s^{-1}) at a depth of 700 m, as observed by the two CTD surveys.

encounter changes in the direction and intensity of the mean flow such that some or all of the three waves can become unstable and develop into intense eddies. This is because, as the mean current becomes stronger, the region of instability becomes larger; also as the flow direction changes, so does the location of the unstable region.

McWilliams and Flierl (1976) have fitted planetary waves to the MODE-0 and MODE-1 datasets, separately. While the former contained only current-meter records from seven separate moorings and mostly from beneath the main thermocline, the latter was a much larger and more uniform dataset, obtained from a variety of instruments: current meters, moored temperature sensors, CTDs and STDs, and SOFAR floats. The best MODE-0 fit has a high correlation of ≈ 0.8 with the data and accounted for over half ($\approx 60\%$) of the data energy. It consisted of a pair of barotropic waves and no baroclinic waves, propagating in the absence of mean flow. The reason for not being able to observe any baroclinic waves is that MODE-0 was primarily an experiment in the lower layer (below the main thermocline) where the barotropic-mode kinetic energy dominates. Nonlinear interactions within the MODE-0 wave fit were found to be weak: forced wave amplitudes predicted by the weakly nonlinear theory are about 20% of the primary wave amplitudes. On the other hand, both barotropic and baroclinic waves were observable by the MODE-1 array that contained both adequate current and temperature measurements. The best MODE-1 fit, having a correlation of ≈ 0.7 and accounting for one-half of the data energy, has a pair of barotropic and a pair of first-baroclinic waves, again propagating in the absence of mean flow. However, nonlinear interactions were found to be of marginal but uncertain importance within the MODE-1 fit: forced wave amplitudes were predicted to be large and comparable to the primary wave amplitudes, but by searching in the data for the forced waves with the given frequencies and wavenumbers, no significant energy has been found in them. To explain this, McWilliams and Flierl suggested empirically that the nonlinear transfers of energy might have acted in such a way as to preserve crucial features of the linear solution. From the results of the MODE and our wave fits, we can summarize the dynamics of the mesoscale motion in the general area where MODE and the Ocean Tomography Experiment were conducted as follows:

1) The motion appears to be dominantly wavelike: planetary waves have consistently accounted for more than one-half of the total energy observed in different places and during different time periods.

2) The vertical structure is dominated by the barotropic and first baroclinic modes, with the latter containing the greatest fraction of the available potential energy among all the vertical modes.

3) The space–time behavior of the motion is well predicted by the dispersion relation, i.e. linear dynamics.

4) Most of the waves observed by the three fits have westward group velocities, suggesting that waves originate in the east.

5) The phase propagation is generally westward, and the wavelengths of the propagating baroclinic waves are typically a magnitude of a few hundreds of kilometers.

6) Subinertial oscillations with frequencies higher than the cutoff frequency of dispersive planetary waves have been observed, particularly in the moored temperature records of the Ocean Tomography Experiment (see Fig. 8), indicative of the existence of forced planetary waves.

7) Locally, the presence of a westward mean flow can reduce the interactions of the dispersive planetary waves by increasing the phase velocities.

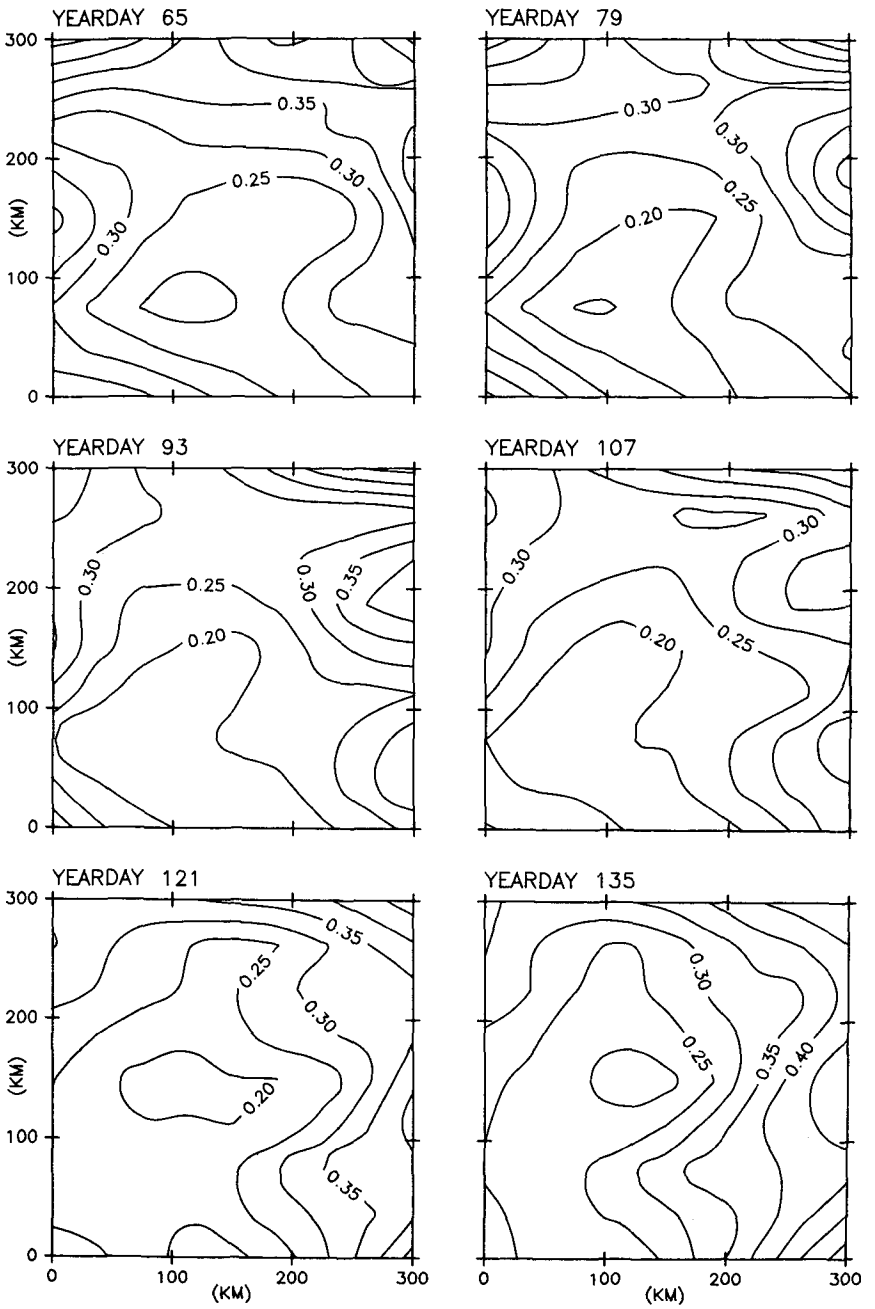

FIG. 11. A time sequence of maps of rms errors (in m s^{-1}) of the optimally estimated sound speed perturbations in the wave field at a depth of 700 m.

TABLE 3. Magnitudes of the phase and particle velocities of the primary dispersive waves. The quantity in parentheses is the phase speed associated with the same wave in the absence of mean current.

Wave (i)	Phase speed (cm s^{-1})	Wave-induced current (cm s^{-1})
1	6.1 (2.2)	2.2
2	3.4 (2.2)	4.0
3	18.3 (10.5)	1.8

5. Conclusions

We have clearly identified in the data the presence of three first baroclinic-mode planetary waves superimposed on a large-scale (i.e. horizontally uniform), vertically sheared current. The waves are found to be linear (i.e. slightly interacting and stable); they account for 78% of the data variance and are highly correlated with the data (correlation of 0.88). The model provides

TABLE 4. Pressure amplitudes of the primary and secondary waves.

Interacting primary waves i–j	Wave amplitudes (10^5 kg km^{-1} s^2)				Ratio of rms forced to primary wave amplitudes
	Primary waves		Forced waves		
1–2	0.598	1.236	0.035	0.014	0.02
1–3	0.598	0.935	0.023	0.330	0.30
2–3	1.236	0.935	0.044	0.155	0.10

a unifying picture and dynamical interpretation of the evolution of the temperature (or sound speed) field over the two and a half month duration of the experiment.

Of course, one can never prove a model to be absolutely correct; it can only be shown to perform better (or worse) than others. Although other models have been tried, including nonadvective propagation, resonant interaction and different numbers of waves, the results presented here constitute our best fit. It has all the desirable features: it is plausible, dynamically consistent, the estimates are well determined, etc.

Even if a model explains the data well, other processes may take place which are not seen by the observing system. This is the case here, in particular with respect to weak or short baroclinic waves, which could have existed in addition to those identified but could not be detected due to insufficient resolution. This is also the case with respect to shallow fluctuations and barotropic motions. The acoustic array, with one-way transmissions, can only detect baroclinic motions, and likewise for the moored temperature sensors and CTD surveys. Only the current meters could provide information on the barotropic component; but being rather sparse and closely spaced, they could not possibly be used as a wave detector. In a similar way, the MODE-0 fit of McWilliams and Flierl (1976) was essentially barotropic, because the current meters used were from below the main thermocline where the kinetic energy in the baroclinic modes is weak. As mentioned above, the float data analyzed by Price and Rossby (1982) likewise contained only the barotropic component. Future tomographic arrays using "reciprocal shooting" will detect currents and constitute more complete systems (Worcester et al., 1985).

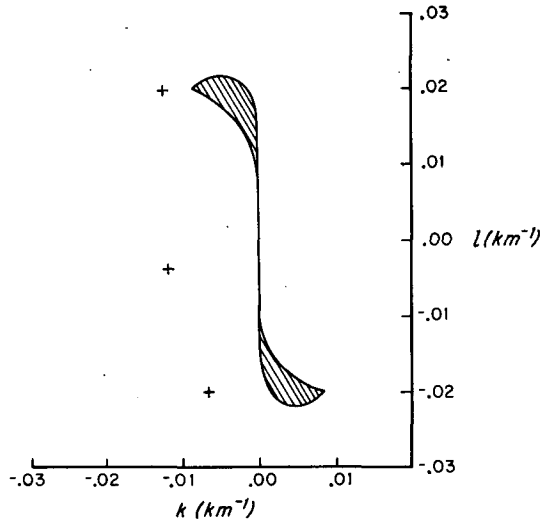

FIG. 12. The stability of the estimated mean flow. The observed wave disturbances (+) are outside the region of instability (shaded area) in the wavenumber domain.

Even though the observing system deployed during the 1981 experiment could not measure currents directly, our wave fit reveals the existence of large-scale, rather weak, vertically sheared horizontal currents. This observation is made possible by the strong constraint imposed by this current on the space–time behavior of the evolving field, through Doppler shift of the wave-frequency.

Since acoustic methods of monitoring mesoscale variability are relatively new, it is perhaps useful to compare the results given here to those obtained either by pure acoustics or by pure "conventional" means. A detailed discussion has been given by Chiu (1985), which can be summarized as follows: if we redo our wave fit using only the acoustic data, the results are very similar to those of Fig. 9, but with an estimated uncertainty (error variance) twice as large. Nonetheless, these errors are half the size of those daily estimates obtained by Cornuelle et al. (1985) for any given day. This shows the advantage of doing, as we have here, a "time-dependent" inversion which takes into account the temporal continuity and the dynamics of the field. The wave parameters obtained in a "pure acoustic" inversion are not very stable, because of the rather large signal produced by the untracked mooring motions instead of by the waves, but this can be corrected in future instrumentation. On the other hand, in this particular example, the temporally, widely spaced CTD surveys and the spatially, sparsely spaced moored temperature arrays could not resolve the waves. The tomographic system, however, has placed a much more stringent space–time constraint on the solution of the field by its observations.

Acknowledgments. We have benefited greatly from many stimulating discussions with Bruce Cornuelle,

Jim Lynch, Robert Spindel and Carl Wunsch. Special thanks to the Ocean Tomography Group for providing the dataset. Our thanks also go to the two reviewers of this article for their thoughtful and helpful comments. This work was supported by the Office of Naval Research under Contract N00014-82-C-0019.

APPENDIX A

Linearity Of Acoustic Travel Times

The time required for a pulse signal to transmit through a ray path connecting a source to a receiver in a perturbed and moving medium is given by

$$\bar{t}+\delta t=\int_{\chi+\delta\chi}[\bar{c}+\delta c+\mathbf{v}\frac{d}{ds}(\chi+\delta\chi)]^{-1}ds \quad \text{(A1)}$$

where the quantity in the bracket is often referred to as the ray speed (Uginčius, 1970). In (A1), s is the arc length along the ray path, the nominal quantities $\bar{t}$ and $\chi(s)$ are respectively the travel time and ray trajectory in an unperturbed and motionless state (i.e. the reference state), and δt and $\delta\chi(s)$ are respectively their deviations caused by the flow field $\mathbf{v}$ and the perturbations δc in sound speed. In general, travel times are perturbed in a very complicated manner. Both the sound speed perturbations and currents can affect travel times directly. They can also affect travel times indirectly by changing the ray trajectories. However, Hamilton et al. (1980) have shown that for any stable ray (that is, any ray that exists in the reference state and does not disappear or alter drastically its geometry in the perturbed state) and for weak horizontal variations in δc and $\mathbf{v}$ the contribution of $\delta\chi$ and δt is of order higher than that contributed explicitly by the changes in the ray speed. Therefore, they concluded that the perturbed travel times may be evaluated along the nominal ray trajectories without losing much accuracy. For most oceanic fluctuations $|\delta c| \gg |\mathbf{v}|$ and hence $\mathbf{v}$ may also be neglected in the travel-time evaluation. By further neglecting terms of order $(\delta c/c)^2$, δt may be approximated by (1).

The use of the approximate relation (1) for linear inversion was suggested by Munk and Wunsch (1979). Cornuelle (1983) and Mercer and Booker (1983) have considered its validity in numerical experiments; while the former found confirming evidence for typical mid-ocean eddies in long-range transmissions, the latter found conflicting evidence for the case of a warm eddy at temperature changes greater than 1°C and 1000 km propagation range. These conflicting results only suggest to us that the linear approximation (1) must be reassessed for the case of planetary waves. In doing so, planetary waves that produce δc of order 5 m s^{-1} and $\mathbf{v}$ of order 5 cm s^{-1} in the upper ocean were simulated; these values are typical of the open ocean. The results, which confirm the validity of (1) for a transmission range of 300 km, are summarized as follows:

1) Travel-time perturbations of order 30 ms are observed.

2) Ray paths are practically unperturbed. The vertical and horizontal changes of their geometries are of order 50 m and ½ km, respectively. These changes are small compared to the scales of the wave perturbations. Furthermore, negligible errors of one to three milliseconds are introduced in δt when the nominal ray paths are used for the calculation.

3) Current effects are negligible. Travel-time perturbations created by the flow field are one to two milliseconds.

4) Although the combined error created by the assumption of stationary ray paths and the neglect of current effects can be up to 15% of the signal, the estimate of a few wave parameters is not affected when a large number of travel-time data are available.

APPENDIX B

Vertical Structure

Strong evidence exists in previous observations that the vertical structure of the oceanic fluctuations in the MODE area is predominantly composed of only a few of the lower vertical modes. McWilliams and Flierl (1975) have shown that over 90% of the kinetic energy in MODE was contained in two empirical orthogonal vertical modes that closely resemble the barotropic and the first baroclinic modes of Rossby waves, while Richman et al. (1977) find that 90% of the potential energy, again in MODE, was contained in the first three baroclinic modes, with 65% of the energy being contained in the first mode alone. Therefore, we shall use the dynamical modes for our wave models, which are solution of the eigenvalue problem (LeBlond and Mysak, 1978; Pedlosky, 1979):

$$\frac{d}{dz}\left(\frac{\bar{f}^2}{N^2}\frac{d}{dz}f_i\right)+\lambda_i f_i, \quad i=0,1,2,\cdots \quad \text{(B1)}$$

with boundary conditions

$$\frac{d}{dz}f_i(0)=\frac{d}{dz}f_i(-D)=0 \quad \text{(B2)}$$

and satisfy the orthonormal condition

$$\frac{1}{D}\int_{-D}^{0}f_i(z)f_j(z)dz=\begin{cases}1, & i=j\\ 0, & i\neq j.\end{cases} \quad \text{(B3)}$$

In (B1)–(B3), $N(z)$, $\bar{f}$, D, $f_i(z)$ and λ_i are the buoyancy frequency, the Coriolis parameter, the ocean depth, the ith eigenfunction (vertical mode) for pressure (or geostrophic velocity), and the corresponding eigenvalue, respectively.

Assuming that the sound speed fluctuations are created by the vertical displacement of the surfaces of constant sound speed, the sound speed perturbation modes are given by

$$g_i(z) = h_i(z)\bar{f}^{-1}\left[\frac{d}{dz}\bar{c}(z) - \frac{d}{dz}c_A(z)\right] \quad i = 1, 2, \cdots$$

where

$$h_i = D\bar{f}^2 N^{-2}\frac{d}{dz}f_i \quad i = 1, 2, \cdots$$

are the vertical displacement modes, and $dc_A(z)/dz$ is the adiabatic sound speed gradient. The first three sound speed perturbation modes, normalized to have maxima of unity, are displayed in Fig. 4. The barotropic mode [i.e. $f_0(z)$] produces negligible displacement and sound speed perturbations.

The surveyed sound speed perturbation profiles (the observed deviations from $\bar{c}$) can be decomposed as

$$\delta c_j^{\mathrm{CTD}}(z) = \sum_i d_{ij} g_i(z) \quad j = 1, 2, \cdots$$

where d_{ij} represents the weight of g_i in the jth observed profile $\delta c_j^{\mathrm{CTD}}$ and can be easily computed using the fact that the $\bar{c}N^{-1}g_i$ (or Nh_i) functions are orthogonal to each other.

To investigate the modal content of the field, we have made the following calculations for each of the CTD casts:

$$P_{Mj} = \left(1 - \frac{\int |\delta c_j^{\mathrm{CTD}} - \sum_{i=1}^{M} d_{ij} g_i|^2 dz}{\int |\delta c_j^{\mathrm{CTD}}|^2 dz}\right) \times 100\%, \quad M = 1, 2, 3$$

where P_{Mj} is the percentage of the energy in $\delta c_j^{\mathrm{CTD}}$ contained in the first M baroclinic modes alone. We found P_{1j} to be 50% to 90% in all the casts, in agreement with Richman et al. (1977). We also found that the contributions of the second and third modes are insignificant in this region, there being less than a 5% increase in the P_{2j} and P_{3j} from P_{1j}, showing the dominance of the lowest baroclinic mode.

APPENDIX C

Measurement Models and Mooring Motion

For the qth modal-amplitude datum a_q^0 observed at $(x, y, t) = (x_q, y_q, t_q)$ and the kth datum $\delta c_{lk}^0 = \delta c_l^0$ $(t = t_k)$ in the lth δc time series (converted from the temperature record) observed at $(x, y, z, t) = (x_l, y_l, z_l, t_k)$, the corresponding measurement processes can be expressed simply as

$$a_q^0 = a_q^m(\mathbf{p}) + v_q^a$$

$$\delta c^0 = \delta c_{lk}^m(\mathbf{p}) + v_{lk}^{\delta c}$$

where

$$a_q^m = \int_{-D}^{0} \delta c^m(x_q, y_q, z, t_q) \cdot g_1(z) dz$$

$$\delta c_{lk}^m = \delta c^m(x_l, y_l, z_l, t_k)$$

are the signals, and v_q^a and $v_{lk}^{\delta c}$ are the experimental noise in a_q^0 and δc_{lk}^0, respectively. In general, the experimental noise that accounts for all the noise in the observing system is the sum of model and measurement errors. While the former error represents that part of the signal due to processes not accounted for in our model (for instance higher modes, tides, internal waves, etc.), the latter is purely of instrumental origin.

In addition to the baroclinic waves, mean current, background oceanic fluctuations, and measurement errors, the relative motions and the uncertainty in the nominal positions of the acoustic moorings also contribute to the observed travel-time perturbations. In fact, the latter two contributions were dominant. If one were to model these mooring-position related travel-time perturbations as part of the experimental noise, the δt time records would suffer a vanishingly small ratio of signal to noise. In order to improve the quality of the δt data, as suggested by Cornuelle (1983), the mooring-position related travel-time perturbations must also be modeled as signals, implying that the uncertainty in the mooring positions must also be expressed as unknown parameters in the acoustic measurement equations.

A set of relative mooring-displacement data was available from the acoustic navigation systems. The tracking data had already been applied to eliminate the signal produced by some of the mooring motions in the travel-time data. But since the tracking time records contain large gaps resulting from occasional malfunction of the tracking instruments, the untracked or unknown horizontal displacements together with the uncertainty in the horizontal nominal positions of the moorings must still be parameterized. The vertical translations of the acoustic sources and receivers were small (of order 50 m) and produced very little travel-time perturbations (of order 1 ms); therefore, they need not be parameterized.

Let us consider the jth ray path connecting the mth source Sm to the nth receiver Rn. According to Cornuelle (1983), the additional time required for the acoustic wave front to travel from Sm to Rn along the path due to a small elongation δR (say of order 1 km) of the horizontal distance separating Sm and Rn can be expressed, to lowest order, as

$$\delta t_j^{\delta R} = r_j \delta R$$

where r_j is the corresponding ray parameter, i.e. the cosine of the transmission (arrival) angle divided by the sound speed at the source (receiver); r_j is a conserved quantity along the ray. Let the unknown horizontal-displacement vectors at time t_k and the time-independent errors on the assumed nominal horizontal-position vectors of Sm and Rn be $[\delta x_{Sm}(t_k), \delta y_{Sm}(t_k)]$ and $[\delta x_{Rn}(t_k), \delta y_{Rn}(t_k)]$, and $(\Delta x_{Sm}, \Delta y_{Sm})$ and $(\Delta x_{Rn}, \Delta y_{Rn})$, respectively. It then follows that the corresponding $\delta t_j^{\delta R}$ at time t_k is given by

$$\delta t_j^{\delta R}(t_k) = r_j \cos\phi_{mn}[\Delta x_{Rn} - \Delta x_{Sm} + \delta x_{Rn}(t_k) - \delta x_{Sm}(t_k)] + r_j \sin\phi_{mn}[\Delta y_{Rn} - \Delta y_{Sm} + \delta y_{Rn}(t_k) - \delta y_{Sm}(t_k)]$$

where ϕ_{mn} is the direction of the horizontal line of transmission from *Sm* to *Rn*, measured in degrees (positive anticlockwise) with respect to the x-axis, i.e. east axis.

We are now in a position to write down the acoustic model equations. For the travel-time perturbation $\delta t_{jk}^0 = \delta t_j^0$ ($t = t_k$) observed from the jth ray path at time t_k, the corresponding equation can be cast symbolically as

$$\delta t_{jk}^0 = \delta t_{jk}^m[\mathbf{p}, \Delta x_{Sm}, \Delta y_{Sm}, \Delta x_{Rn}, \Delta y_{Rn}, \delta x_{Sm}(t_k), \delta y_{Sm}(t_k), \delta x_{Rn}(t_k), \delta y_{Rn}(t_k)] + v_{jk}^{\delta t}$$

where $v_{jk}^{\delta t}$ represents the experimental noise in δt_{jk}^0. The signal δt_{jk}^m can be written as the sum of two parts such that

$$\delta t_{jk}^m = \delta t_{jk}^p + \delta t_{jk}^{\delta R}$$

where $\delta t_{jk}^{\delta R} = \delta t_j^{\delta R}(t_k)$ and δt_{jk}^p is the signal induced by the waves and mean flow which, following (1), can be expressed as

$$\delta t_{jk}^p = \int_{\chi_j(s)} \frac{-\delta c^m(\mathbf{x}, t_k; \mathbf{p})}{\bar{c}(z)^2} ds$$

with χ_j denoting the nominal trajectory of the jth ray.

REFERENCES

Backus, G. E., and J. F. Gilbert, 1970: Uniqueness in the inversion of inaccurate gross Earth data. *Phil. Trans. Roy. Soc. London,* **A266,** 123–192.

Bard, Y., 1974: *Nonlinear Parameter Estimation.* Academic Press.

Bernstein, R. L., and W. B. White, 1974: Time and length scales of baroclinic eddies in the central North Pacific Ocean. *J. Phys. Oceanogr.,* **4,** 613–624.

Chiu, C. S., 1985: Estimation of planetary wave parameters from the data of the 1981 Ocean Acoustic Tomography Experiment. Ph.D. thesis, Woods Hole Oceanographic Institution/Massachusetts Institute of Technology.

Cornuelle, B., C. Wunsch, D. Behringer, T. Birdsall, M. Brown, R. Heinmiller, R. Knox, K. Metzger, W. Munk, J. Spiesberger, R. Spindel, D. Webb and P. Worcester, 1985: Tomographic maps of the ocean mesoscales. Part I: Pure Acoustics. *J. Phys. Oceanogr.,* **15,** 133–152.

Cornuelle, B., 1983: Inverse method and results from the 1981 Ocean Acoustic Tomography Experiment. Ph.D. thesis, Woods Hole Oceanographic Institution/Massachusetts Institute of Technology.

Emery, W. J., and L. Magaard, 1976: Baroclinic rossby waves as inferred from temperature fluctuations in the eastern Pacific. *J. Mar. Res.,* **34,** 365–385.

Eriksen, C. C., 1985: Moored observations of deep low frequency motions in the central Pacific Ocean: Vertical structure and interpretation as equatorial waves. *J. Phys. Oceanogr.,* **15,** 1085–1113.

Fletcher, R., and M. J. D. Powell, 1963: A rapidly convergent descent method for minimization. *The Comput. J.,* **6,** 163–168.

Flierl, G. R., 1978: Models of vertical structure and calibration of two-layer models. *Dyn. Atmos. Oceans,* **2,** 341–381.

Hamilton, G., W. L. Siegmann and M. J. Jacobson, 1980: Simplified calculation of ray-phase perturbations due to ocean-environmental variations. *J. Acoust. Soc. Amer.,* **67,** 1193–1206.

Hogg, N. G., 1980: Observations of internal Kelvin waves trapped round Bermuda. *J. Phys. Oceanogr.,* **10,** 1353–1376.

——, 1981: Topographic waves along 70°W on the continental rise. *J. Mar. Res.,* **39,** 627–649.

Holloway, G., 1980: Oceanic internal waves are not weak waves. *J. Phys. Oceanogr.,* **10,** 906–914.

Koshlyakov, M. N., and Y. M. Grachev, 1973: Mesoscale currents at a hydrophysical polygon in the tropical Atlantic. *Deep-Sea Res.,* **20,** 507–526.

LeBlond, P. H., and L. A. Mysak, 1978: *Waves in the Ocean.* Elsevier Scientific.

Longuet-Higgins, M. S., and A. E. Gill, 1967: Resonant interactions between planetary waves. *Proc. Roy. Soc. London,* **A229,** 773–784.

Mercer, J. A., and J. R. Booker, 1983: Long-range propagation of sound through oceanic mesoscale structures. *J. Geophys. Res.,* **88,** 689–700.

McWilliams, J., and A. Robinson, 1974: A wave analysis of the Polygon array in the tropical Atlantic. *Deep-Sea Res.,* **21,** 359–368.

——, and G. R. Flierl, 1975: Quasigeostrophic wave analyses. *Dynamics and the Analysis of MODE-1,* A. R. Robinson, Ed., MIT Press.

——, and ——, 1976: Optimal quasi-geostrophic wave analyses of MODE array data. *Deep-Sea Res.,* **23,** 285–300.

Medwin, H., 1975: Speed of sound in water: A simple equation for realistic parameters. *J. Acoust. Soc. Amer.,* **58,** 1318–1319.

Mooers, C. N. K., 1975: Sound-velocity perturbations due to low-frequency motions in the ocean. *J. Acoust. Soc. Amer.,* **57,** 1067–1075.

Muller, P., and G. Siedler, 1976: Consistency relations for internal waves. *Deep-Sea Res.,* **23,** 613–628.

Munk, W., and C. Wunsch, 1979: Ocean acoustic tomography: A scheme for large-scale monitoring. *Deep Sea Res.,* **26A,** 123–161.

Ocean Tomography Group, 1982: A demonstration of ocean acoustic tomography. *Nature,* **299,** 121–125.

Pedlosky, J., 1979: *Geophysical Fluid Dynamics.* Springer-Verlag.

Piips, T., 1967: Precision sound velocity profiles in the ocean. Vol. II, The Sound Channel in the Bermuda–Barbados Region, April–July 1964. Tech. Rep. No. 4, Lamont Geological Observatory, Columbia University.

Price, J. F., and H. T. Rossby, 1982: Observations of barotropic planetary waves in the North Atlantic. *J. Mar. Res.,* **40,** Suppl., 543–558.

Richman, J. G., C. Wunsch and N. G. Hogg, 1977: Space and time scales of mesoscale motion in the western North Atlantic. *Rev. Geophys. Space Phys.,* **15,** 385–420.

Sanford, T. B., 1975: Observations of the vertical structure of internal waves. *J. Geophys. Res.,* **80**(27), 3861–3871.

Spindel, R. C., 1979: An underwater acoustic pulse compression system. *IEEE Tran., Acoustic, Speech and Signal Proc.,* Vol. ASSP-27, No. 6, 723–728.

Tarantola, A., and B. Valette, 1982: Generalized nonlinear inverse problems solved using least-squares criterion. *Rev. Geophys. Space Phys.,* **19,** 219–232.

Thompson, R. O. R. Y., 1971: Topographic Rossby waves at a site north of the Gulf Stream. *Deep-Sea Res.,* **18,** 11–19.

Uginčius, P., 1970: Ray acoustics and Fermat's Principle in a moving inhomogenous medium. *J. Acoust. Soc. Amer.,* **51,** 1759–1763.

Weisberg, R. H., A. Horigan and C. Colin, 1979: Equatorially trapped Rossby–gravity waves propagation in the Gulf of Guinea. *J. Mar. Res.,* **37,** 67–86.

White, W. B., 1977: Annual forcing of baroclinic long waves in the tropical North Pacific Ocean. *J. Phys. Oceanogr.,* **7,** 50–61.

Worcester, P. F., R. C. Spindel and B. M. Howe, 1985: Reciprocal acoustic transmissions: Instrumentation for mesoscale monitoring of ocean currents. *IEEE J. Oceanic Eng.,* **OE10**(2), 123–137.